First principles analysis on the nucleation interface of $La_2O_3(1\bar{1}0)$/ NbC$(1\bar{1}0)$

Wenwei Song[a] , Qizhen He[a] , Yuguo Zhuo[b]* , Wei Shao[a] , Silong Zhang[a] , Xuejun Ren[c] , Qingxiang Yang[a],*

[a] State Key Lab of Metastable Materials Science & Technology, Hebei key lab for optimizing metal product technology and performance, College of Materials Science & Engineering, Yanshan University, Qinhuangdao 066004, PR China [b] Department of Environmental Engineering, Hebei University of Environmental Engineering, Qinhuangdao 066102, PR China [c] School of Engineering, Liverpool John Moores University, Liverpool L3 3AF, UK

ABSTRACT: Niobium carbide (NbC), as a reinforcement phase, has been applied in the alloy to enhance its service life. It is important to refine the NbC in the alloy. In this paper, the nucleation interface of $La_2O_3(1\bar{1}0)$/NbC$(1\bar{1}0)$ was analyzed and the mechanism of NbC refined by La_2O_3 was investigated by first principles. Firstly, the mismatch degree of La_2O_3/NbC interface was calculated. According to the surface convergence, the interface models of La_2O_3/NbC were established. Then, the combined work and energy of the La_2O_3/NbC interfaces were calculated. Finally, the interface bonding properties were analyzed by the charge density, differential charge density and projected density of states. The results show that the mismatch degree of $La_2O_3(1\bar{1}0)$/NbC$(1\bar{1}0)$ interface is smallest, which is 7.1%. $La_2O_3(1\bar{1}0)$ and NbC$(1\bar{1}0)$ lattice planes were selected to establish four kinds of interface models, which are named as O-Hollow, O-Interface, OLa-Hollow and OLa-Interface in turn. The adhesive work of O-Hollow interface is the largest, which is 0.995J/m^2. And its interface energy is the smallest, which is 3.055J/ m^2. Meanwhile, the bonding types of O-Hollow interface are mainly a combination of La-C and Nb-O bonds. In summary, La_2O_3 can be as a moderate effective heterogeneous nucleus of NbC, then NbC be refined by La_2O_3

1. Introduction

Because of its high melting point and high hardness, Niobium carbide (NbC) has been applied in the alloy to enhance the service life of the engineering workpiece [1–3]. During the solidification process of the alloy, NbC can be precipitated from the liquid metal firstly, as a reinforcement phase, to reinforce the comprehensive mechanical properties of the alloy [4–7]. Zhang et al. [8] found that, the ceramic phase NbC is preferentially precipitated in hypereutectic high chromium cast iron (HHCCl) with the purpose of refining the primary M7C3 carbide. Lu et at. [9] prepared Nb-reinforced Co50 composite coating by plasma cladding experiment. The results show that NbC can be preferentially precipitated at the grain boundary, leading to the refinement of grain and microstructure. Zeng et al. [10] added an appropriate amount of Nb in high-strength low-alloy steel (HSLA), and the results showed that NbC inhibits the growth of austenite grains. From about reports, it can be found that the reinforcement effect in the alloy is related with NbC dimension closely. As it has a smaller size when it solidifies from the liquid phase, and the reinforcement effect of NbC on the alloy is remarkable. Therefore, it is important to refine the NbC when it is precipitated from the solidification process of the alloy. Because of the unique atomic structure and properties, rare earth (RE) elements have been applied in purification, modification and refinement of the alloys [11–13]. During solidification of the alloy, RE element can react not only with the oxygen and impurity element in liquid, to form the RE oxides or RE compounds to purify the alloys and modify the inclusions [14,15], and it can also be as heterogeneous nucleus of the solidified structure and refine it, so as to improve the comprehensive performance of the alloys

[16–18]. Zhuang et al. [19] prepared the Ni-based coating on the surface of Ti-6Al-4 V alloy by laser cladding method. With the addition of element Ce, the phase composition of the coating includes TiC, TiB2, Ti2N, α-Ti and Ce_2O_3. Among them, Ce_2O_3 can serve as the TiC heterogeneous nucleus, which can effectively refine TiC and improve the micro-hardness and wear resistance of the coating. Hantzsche et al. [20] added appropriate elements Ce, Nd and Y to magnesium alloy, which can inhibit the growth of grain in the annealing process and achieve the purpose of refining grain.

Among RE elements, element La as the representative one, has attracted extensive attention in the research of new materials due to its abundant reserves in nature and outstanding performance [21,22]. Jiang et al. [23] studied the effect of element La on the microstructure, tensile properties and fracture behavior of A357 alloy. The results showed that the addition of La element can refine the primary α-Al phase and eutectic Si grains, and the tensile properties of the alloy are greatly improved. Zhou et al. [24] proved by experimental that La2O3 can refine primary M7C3 carbides in hypereutectic Fe-Cr-C alloy. Jiao et al. [25] found that La_2O_3 can refine γ-Fe in austenitic stainless steel.

It has been reported that due to refinement of NbC, the service life of the alloy can be further improved by adding RE oxides [26,27]. Shi et al. [28] added Y_2O_3 to the hypereutectic Fe-Cr-C alloy simultaneously, and found that Y_2O_3 can refine NbC. Inspired by the above research work, we try to add La_2O_3 and NbC into the hypereutectic Fe-Cr-C- alloy simultaneously, and found that $LaAlO_3$ can effectively refine NbC [29]. However, whether La_2O_3 can directly refine NbC in the above alloys has not been reported. Meanwhile, because the sizes of La_2O_3 and NbC are small, and their amount are small too, it is difficult to explain the mechanism of NbC refined with La_2O_3 by experimental method.

First-principle method based on density functional theory has attracted extensive attention in interface research [30,31]. Guo et al. [32] studied the tensile and shear deformation of ZrO_2(111)/Ni(111) at the ceramic-metal (C-M) interface by the first-principle method, and calculated the ideal mechanical strength of the ZrO_2(111)/Ni(111) interface. Ling et al. [33] systematically studied the effects of non-metallic (sulfur) doping, defect engineering and interface coupling on the electronic structure of g-C_3N_4 and their synergistic effects through first-principle method, and confirmed the possibility of doping, defect engineering and interface coupling in photo-catalysis. Xue et al. [34] studied the binding mechanism of Ti and Al_2O_3, and the bonding phenomenon at the interface by first principles. Therefore, it is feasible to investigate the mechanism of NbC refined by La_2O_3 by first principles.

In this paper, the interfacial relationship between La_2O_3/NbC and the possibility of La_2O_3 as NbC heterogeneous nucleus was investigated by first-principle method. Firstly, the lattice mismatch degree of La_2O_3/ NbC interface was calculated. Then, the interface models of La_2O_3/NbC were established, the corresponding interface adhesive work and interface energy were calculated, and the interface binding strength and nucleation resistance were determined. Meanwhile, the charge density, differential charge density and the projected density of states of the interface were calculated. The bonding types were further analyzed. Finally, the possibility of La_2O_3 as heterogeneous nucleus of NbC was discussed, and the mechanism of NbC refined by La_2O_3 was proposed.

Calculation details

All the work in this paper adopted the first principles based on density functional theory (DFT) and was realized through VASP (Vienna Ab-intio Simulation Package) [35–37]. With Perdew Burke Ernzerh (PBE Approximation) under General Gradient Approximation (GGA), exchange association effects between electrons were described [38]. The interaction between ions and electrons in the system was processed by using Projector-Augmented Wave (PAW) [39–41], and K points in Brillouin region were generated automatically by using Monkhorst-Pack (M-P) method with γ as the center [42]. The pseudopotential information of the required elements generated by vaspkit [43] is as follows: La, O, Nb_sv and C. For structural optimization, the position of all atoms was relaxed freely, and the energy change value and force converge to 1×10^{-5} eV/atom and 0.01 eV/A, respectively.

The initial structural model used for the calculation is shown in Fig. 1. Fig. 1(a) is the crystal model of La_2O_3, which belongs to the P321 space group [44,45], and the lattice constants after full relaxation are a=b= 3.94 Å and c= 6.13 Å. Fig. 1(b) is the crystal model of NbC, which belongs to the sodium chloride structure of the FM-3 M space group [46]. The optimized lattice constant is a=b=c= 4.40 Å. In the whole process of crystalline models optimization, the selected plane wave truncation energy Ecut value and K point network in Brillouin region are 500 eV and 9 × 9 × 9, respectively. In the surface convergence test and the interface relaxation process, the E_{cut} value and K point are 500 eV and 9 × 9 × 1, respectively.

3. Results and analysis

3.1. Structural and mechanical properties of La2O3

The calculated results of band and density of states (DOS) of La_2O_3 are shown in Fig. 2. Fig. 2(a) is the band diagram of La_2O_3, and the dotted line is the position of the Fermi level. It can be seen that the band does not cross the Fermi level, and there is a certain band gap between the valence band and the conduction band, with a band gap of 3.81 eV. Since the valence band top and conduction band bottom of La_2O_3 are not directly aligned, it indicates that La_2O_3 has the characteristics of indirect band gap semiconductor.

Fig. 2(b) is the total DOS and the projected density of states(PDOS) of each atomic orbital. La_2O_3 has no PDOS peak at the Fermi level, which indicates that it has no metallic properties. In the range of − 17 eV to − 10 eV, there is a certain orbital resonance and hybridization between the s orbital of O atom and the p orbital of La atom, which indicates that the chemical bond has a certain covalent bonding property. From 3 eV to the Fermi level of PDOS peak, mainly comes from the O-p orbital contribution. O-p orbital and La-d orbital resonance occurs. The La atom of peak strength is very weak, which indicates that La outer electrons of the atoms transfer to the O atom with greater electronegativity. The PDOS peaks of gravity for La-d orbitals is different from that of O-p orbitals, it indicates that they have strong ionic bonds. Therefore, the chemical bond in the structure of La_2O_3 is a mixture of covalent bond and ionic bond.

The elastic matrix of La_2O_3 was calculated by first principles method. The results are as follows:

$$C_{ij}(GPa) = \begin{vmatrix} 201 & 119 & 78 & & & \\ 119 & 201 & 78 & & & \\ 78 & 78 & 132 & & & \\ 32 & -32 & & 56 & & \\ & & & & 56 & 32 \\ & & & & 32 & 41 \end{vmatrix}$$

According to the calculation results of the elastic matrix of La_2O_3, the elastic constants and their elastic anisotropy were calculated using the code, which is named as ELATE [47], as shown in Tables 1 and 2. The 2D and 3D anisotropy distributions of Young's modulus, linear coefficient, shear modulus and Poisson's ratio of La2O3 are shown in Fig. 3.

The elastic properties of La2O3 were further analyzed in combination with Table 2 and Fig. 3. Fig. 3(a) is the 2D and 3D anisotropy distribution of Young's modulus of La_2O_3. It can be seen that there is no anisotropy in the distribution of Young's modulus in the x dimension, and the distribution in the y direction is less than 100 GPa. The maximum value of Young's modulus in the z dimension is nearly twice as large as that in the y dimension, and the maximum value can reach 201.49 GPa and the anisotropy value is 4.37. Fig. 3(b) is the 2D and 3D anisotropy distribution of linear coefficient. It can be seen that there is no anisotropy in the distribution of linear coefficient in the x direction, and the distribution is almost the same in the y dimension and the z dimension. Its minimum value is $1.79TPa^{-}1$, the maximum value is $5.44TPa^{-1}$, and the anisotropy value is 3.04. Fig. 3(c) is the 2D and 3D anisotropy distribution of shear modulus of La_2O_3. It can be seen that the distribution of shear modulus in the three-dimensional of x, y, and z is very complicated. The minimum value is 15.36 GPa, the maximum value is 81.80 GPa and the anisotropy value is 5.33. Fig. 3(d) shows the 2D and 3D anisotropy distribution of Poisson's ratio of La_2O_3. It can be seen that the distribution of Poisson's ratio in the three-dimensional is more complicated than that of the shear modulus, but the distribution in the x and y dimensions still has certain regularity. Its minimum value is − 0.16, which is known as negative Poisson's ratio effect. And its maximum value can reach 0.97, and the anisotropic value reaches ∞ . The calculation results of band, DOS and elastic constant of NbC have been reported by reference [29].

3.2. Two-dimensional lattice mismatch

According to Bramfitt two-dimensional lattice mismatch theory [48], the combination of crystal planes with a mismatch degree of less than 12% can form heterogeneous interfaces. The low index lattice planes of La2O3/NbC are selected as $La_2O_3(1\bar{1}0)$/NbC$(1\bar{1}0)$, $La_2O_3(001)$/NbC(100) and $La_2O_3(100)$/NbC(100). The mismatch relationships of above lattice planes were calculated, and the results are listed in Table 3. It can be seen that, the lattice mismatch degree of $La_2O_3(1\bar{1}0)$/NbC$(1\bar{1}0)$ is the smallest, which is 7.1%. So the interface of $La_2O_3(1\bar{1}0)$/NbC$(1\bar{1}0)$ is a semi-coherent interface. It is proved that La_2O_3 can be as the heterogenous nucleus of NbC.

3.3. Establishment of interface models

$La_2O_3(1\bar{1}0)$ and $NbC(1\bar{1}0)$ lattice planes were selected to establish surface models according to the results of two-dimensional lattice mismatch degree. To counteract the interatomic interactions on the surface, a vacuum layer with a thickness of 15 Å is added. The types of $La_2O_3(1\bar{1}0)$ lattice plane includes OLa-Terminated and O-Terminated, and the types of $NbC(1\bar{1}0)$ lattice owns only one type named as NbC-Terminated. Surface models of La_2O_3 and NbC are shown in Fig. 4.

3.3.1. Surface energy of $La_2O_3(1\bar{1}0)$

Before the establishment of La_2O_3/NbC interface models, it is necessary to test the surface convergence of the corresponding surface models. Firstly, the surface models of La_2O_3 need to be fully relaxed. The chemical potential formula of surface models for La_2O_3 is as follows:

$$\mu_{La_2O_3}^{bulk} = 2\mu_{La} + 3\mu_O \quad (1)$$

where μ_{bulk} La_2O_3 is the system energy after structural relaxation of La_2O_3; μ_{La} is the chemical potential of the La atom; μ_O is the chemical potential of the O atom, which is −4.905 eV.

The formula for calculating the surface energy of La_2O_3 is as follows:

$$\sigma_{La_2O_3(1\bar{1}0)} = \frac{1}{2A}(E_{slab} - N_{La}\mu_{La} - N_O\mu_O) \quad (2)$$

where $\sigma_{La2O3(1\bar{1}0)}$ is surface energy of the $La_2O_3(1\bar{1}0)$ surface models; E_{slab} is energy of the surface models with a certain number of atomic layers; A is area of surface models; N_{La}, N_O are numbers of La and O atoms in surface models of $La_2O_3(1\bar{1}0)$. Combining with Eqs. (1) and (2), the final surface energy formula of $La_2O_3(1\bar{1}0)$ is as follow:

$$\sigma_{La_2O_3(1\bar{1}0)} = \frac{1}{2A}[E_{slab} - \frac{1}{2}N_{La}\mu_{La_2O_3}^{bulk} + \left(\frac{3}{2}N_{La} - N_O\right)\mu_O] \quad (3)$$

Surface convergence test is one of the most common methods to judge that the atomic layer numbers in the surface models have reached to bulk properties. $La_2O_3(1\bar{1}0)$ surface energy of OLa-Terminated and O-Terminated with different termination of layer surface models were calculated by Eq. (3), and their results are listed in Table 4. It can be seen that surface energy of OLa-Terminated surface models converge to 2.07J/m^2 , when the atomic layers reach to 13 layers. For O-Terminated surface models of $La_2O_3(1\bar{1}0)$, its surface energy converges to 1.08 J/ m^2, when the atomic layers reach to 10 layers.

3.3.2. Surface energy of NbC(110)

The NbC(110) surface is non-polar. According to Botteger equation [49], the formula of surface energy is as follows:

$$\sigma_{NbC[1\bar{1}0]} = \frac{1}{2A}(E_{slab}^N - N\Delta E) \quad (4)$$

$$\Delta E = (E_{slab}^N - E_{slab}^{N-2})/2 \quad (5)$$

where $\sigma_{NbC[1\bar{1}0]}$ is surface energy of $N_bC(1\bar{1}0)$ surface models; $E_{slab}^{N}, E_{slab}^{N-2}$ are the energy of the N_{th}-layer and $(N\text{-}2)_{th}$-layer, respectively; N is the number of atomic layers of the surface models. Surface energy of NbC-Terminated for $NbC(1\bar{1}0)$ was calculated by Eqs. (4) and (5), and the results are listed in Table 5.

According to results of surface convergence test, the 13th-layer of OLa-Terminated surface models, the 10th-layer of O-Terminated for $La_2O_3(1\bar{1}0)$surface models and the 11th-layer of NbC-Terminated surface models for $NbC(1\bar{1}0)$ are prepared for subsequent calculations.

3.4. Analysis of interfacial bonding strength and bonding type

Four interface models of O-Hollow, O-Interface, OLa-Hollow and OLa-Interface were established based on above results. Among them, the atoms of the $NbC(1\bar{1}0)$ surface models of the Hollow-type interface are located at the bridge position in the interface, and the atoms of the $NbC(1\bar{1}0)$ surface models of the Interface-type interface are located at the top position in the interface. The top view of the established interface models and its (001) lattice planes are shown in Fig. 5. Relaxation and energy calculations are performed for four interface models with interfacial distances of 1.0–3.0 Å. The transformation relationship between the changes of energy for the interface and the interfacial distance are shown in Fig. 6. Among them, the interfacial spacing corresponding to the O-Hollow interface type is 1.6 Å, the interfacial spacing corresponding to the O-Interface interface model is 2.0 Å, the interface spacing corresponding to the OLa-Hollow interface model is 2.6 Å, and the OLa-Interface interface model is 2.6 Å. The corresponding interfacial spacing is 2.6 Å.

3.4.1. Interfacial bonding properties and nucleation resistance

Adhesive work (W_{ad}) is an important parameter to characterize the bonding strength of the interface. The Wad calculation formula of $La_2O_3(1\bar{1}0)/NbC(1\bar{1}0)$interface models is as follows:

$$W_{ad} = \frac{1}{A}(E_{La_2O_3} + E_{NbC} - E_{La_2O_3/NbC}) \quad (6)$$

where W_{ad} refers to the adhesive work of interface models; A is the area of interface; E_{La2O3}、E_{NbC} is the relaxation energy of surface models; $E_{La2O3/NbC}$ is the relaxation energy of La_2O_3/NbC interface models.

Among them, the calculation results of Wad for four interface models are listed in Table 6. It can be seen that Wad of four interface models is as follows: $Wad_{O\text{-}Hollow} > Wad_{O\text{-}Interface} > Wad_{OLa\text{-}Interface} > Wad_{OLa\text{-}Hollow}$. When Wad is negative, the adhesive force at the interface does negative work, and the energy at the interface is higher, which leads to poor bonding ability. Therefore, the adhesive work of O-Hollow interface model is the largest, which is 0.995 J/m^2 . It indicates that the interfacial bonding ability of O-Hollow interface model is the largest.

Interface energy (γ) is the resistance of interfacial nucleation, and the value of interface energy corresponds to the difficulty of nucleation. The γ calculation formula of $La_2O_3(1\bar{1}0)/NbC(1\bar{1}0)$interface models is as follows:

$$\gamma = \sigma_{La_2O_3} + \sigma_{NbC} - W_{ad} \quad (7)$$

where γ refers to interface energy of $La_2O_3(1\bar{1}0)/NbC(1\bar{1}0)$ interface models; σ_{La2O3} is surface energy of La_2O_3 surface models; σ_{NbC} is surface energy of NbC surface models.

The calculated results of γ for four interface models are listed in Table 7. Among them, the γ of four interface models is as follows: $\gamma_{O\text{-}Hollow} < \gamma_{O\text{-}Interface} < \gamma_{OLa\text{-}Hollow} < \gamma_{OLa\text{-}Interface}$. It can be seen that the γ of the O-Hollow interface model is the smallest, which is 3.055 J/m^2 . Combining calculated results of Wad and γ, the interface models of OHollow have the largest adhesive work and the smallest interface energy, which indicates that O-Hollow owns better adhesive ability and relatively lower interfacial nucleation resistance.

3.4.2. Interfacial bonding type analysis

Charge density and differential charge density were used to calculate and analyze the interface charge density and interatomic bonding mechanism. The differential charge density is calculated by the following formula [50]:

$$\rho_d = \rho_{tot} - \rho_{La_2O_3} - \rho_{NbC} \quad (8)$$

where ρ_d is differential charge density of interface models; ρ_{tot} refers to total charge density of interface models; ρ_{La2O3} is charge density of La_2O_3 in interface models; ρ_{NbC} is charge density of NbC in interface models

The electronic structures of the $La_2O_3(1\bar{1}0)$/NbC$(1\bar{1}0)$ interface models are shown in Fig. 7, where the dotted line indicates the position of the interface. Fig. 7(a) is the charge density diagram of O-Hollow at the (010) plane. Blue to red represent the increase in charge density. It can be seen that the La atoms on the La_2O_3 side at the interface diffuse to the interface, and there is a large interaction between La atoms and C atoms. There is a bonding phenomenon. Fig. 7(a′) is the differential charge density map of O-Hollow at the (010) plane, where positive values (red) indicate charge accumulation, and negative ones (blue) indicate charge loss. It can be seen that the charge density of the 1–2layer atoms at the interface are redistributed and localized characteristics appear. There is a large area of charge accumulation at the interface, the La atoms below the interface have a significant charge depletion phenomenon around the side near the interface, and the C atoms located above the interface have a charge accumulation phenomenon around the side close to the interface. The surrounding charges around La atoms are transferred to the above interface, which indicates that the La atoms have stronger electronegativity and La-C bonds are formed between the interfaces.

Fig. 7(b) is the charge density diagram of O-Interface at the (010) plane. It can be seen that C atoms on the NbC side at the interface diffuse to the interface, and the La atoms below the interface have obvious charge accumulation phenomenon on the side close to the interface. There is a large interaction, accompanied by bonding phenomenon. At the 1–2 layers below the interface, there is a charge accumulation region between La atoms and O atoms, and electrons from La atoms are transferred to O atoms. Fig. 7(b′) is the differential charge density map of O-Interface at the (010) plane. It can be seen that a charge accumulation area is formed at the interface, and there is an obvious charge dissipation area around the La atom near the interface, which indicates that the extra-nuclear electrons around the La atom are transferred to the interface, and La-C bonds are formed between the interfaces.

Fig. 7(c) is the charge density diagram of OLa-Hollow at the (010) plane. It can be seen that the first layer of La atoms on the La2O3 side at the interface diffuses to the interface, which indicates that the La atoms and the C atoms on the NbC side have strong mutual attraction. It indicates that there is a strong chemical bond formation. The La atoms and O atoms on the

lower side of the interface are very close to the C atoms above the interface, which indicates that there are chemical bonds between them. Fig. 7(c′) is the differential charge density map of OLaHollow at the (010) plane. It can be seen that there is a large area of charge accumulation at the interface, and a large area of charge dissipation occurs around the Nb atoms on both sides of the interface, which indicates that some extra-nuclear electrons flow into the interface.

Fig. 7(d) is the charge density diagram of OLa-Interface at the (010) plane. It can be seen that the C atoms on the NbC side at the interface have obvious diffusion phenomenon in the horizontal direction near the first and second layers of the interface, and the stacking mode of the interface structure has been changed greatly. Diffusion to the interface, the distance between La atoms and O atoms is relatively close, and chemical bonds (La-O bonds) are formed between them. Fig. 7(d′) is the differential charge density map of OLa-Interface at the (010) plane. It can be seen that a charge-rich region appears at the interface, and a charge-deficient region appears around the Nb and La atoms on both sides of the interface. Therefore, the extra-nuclear electrons around the Nb atom and the La atom are transferred to the interface, and chemical bonds are formed between the interfaces.

According to analysis results of the interface electronic structure, the atoms in the 1–3 layers at the interface shows obvious localization characteristics. Therefore, the PDOS of atoms in layers 1–3 near the $La_2O_3(1\bar{1}0)$/NbC$(1\bar{1}0)$ interface was analyzed. The calculation results are shown in Fig. 8, in which, the position of the red dotted line in the figure represents Fermi level. It can be seen that the PDOS at the interface is not zero at the Fermi level, which indicates that chemical bonds form at the interface have certain metallic properties. Fig. 8(a) is a PDOS diagram of O-Hollow. It can be seen that DOS near the Fermi level is mainly contributed by La-d, O-s, p and C-p orbitals. PDOS peak of each orbital of O atoms in one layer near the interface is lower than that of O atoms in the second and third layers below the interface. In the range of − 5 eV to − 2.5 eV, the La-d orbital of the subouter layer below the interface resonates with the C-p orbital near the interface, and the contribution of PDOS peak of the C-p orbital is large. From − 17.5 eV to − 12.5 eV, the Nb-p orbital near the interface resonates with the O-s orbital, which indicates the formation of covalent or ionic bonds near the interface.

Fig. 8(b) is a PDOS diagram of O-Interface. It can be seen that on the La_2O_3 side, PDOS of each orbital of O atoms in the layer near the interface is lower than that of the sub-layer and the third layer. Meanwhile, it is observed that from the range of − 14 eV to − 10 eV, the Nb-p and O-s orbitals near the interface, and the C-s near the interface and the La-p orbitals of the sub-external layer below the interface all resonate, which proves that Nb-O bonds and La-C bonds form. Fig. 8(c) is a PDOS diagram of an OLa-Hollow. It can be seen that PDOS peak at the interface is mainly from the contribution of C-p atoms and O-s, and the contribution of PDOS of each atom in the 1–3 layers near the interface is equivalent. And from the range of − 17.5 eV to − 12.5 eV, the O-p orbital near the interface is consistent with the Nb-p orbital peak shape, and the peaks are equivalent. Fig. 8(d) is a PDOS diagram of an OLa-Interface. It can be seen that PDOS peak at the Fermi level mainly comes from the contribution of the La-d orbital. From the range of − 17.5 eV to − 12.5 eV, the O-p orbital near the interface is consistent with the C-p orbital peak shape, and the peaks are equivalent. Combined with the calculation results of the electronic structure and the partial wave density of states at the interface, it is found that Nb-O bonds and La-C bonds are formed at the OHollow and O-Interface interfaces. Combined with the calculation results of the electronic structure and PDOS, it is found that Nb-O bonds and La-C bonds are formed at the OHollow and O-Interface interfaces.

4. Discussion on refinement mechanism

Based on the calculation results of Bramfitt's two-dimensional lattice mismatch degree theory, the lattice mismatch between La_2O_3 and NbC heterogeneous lattice planes is 7.1%, which is between 6% and 12%. It proves that they can form a semi-coherent interface. It indicates that La_2O_3 as the substrate plays a moderate effective nucleation role relative to the nucleation phase NbC, which can be refined by La_2O_3. Combined with the calculation results of the interface bonding strength and the interfacial nucleation resistance, the adhesive work of the O-Hollow interface is the largest, which is 0.995 J/m2 , and the interface energy is the smallest, which is 3.055 J/m^2 . It indicates that this interface type has the strongest interfacial bonding strength and the smallest nucleation resistance, so that La_2O_3 and NbC are more inclined to form an O-Hollow hetero-interface. According to the calculation results of interfacial charge density and PDOS, the bond types of O-Hollow hetero-interface is mainly the combination of La-C and Nb-O bonds.

5. Conclusion

(1) From the band diagram of La_2O_3, it can be seen there is a band gap between the valence band and the conduction band, and its value is 3.81 eV, and La_2O_3 has the characteristics of an indirect band gap semiconductor.

(2) The lattice mismatch degree of La2O3$(1\bar{1}0)$/NbC$(1\bar{1}0)$ interface is 7.1%, which proves that La_2O_3 plays a moderate effective role as the heterogeneous nucleus of the substrate phase NbC, and they can form a semi-coherent interface.

(3) Surface convergence test of the low-index lattice planes for La_2O_3 and NbC indicates that 13th-layer OLa-Terminated surface models of $La_2O_3(1\bar{1}0)$, 10th-layer O-Terminated surface models of $La_2O_3(1\bar{1}0)$, and 11th-layer NbC-Terminated of NbC$(1\bar{1}0)$ reach stability. Four kinds of interface models are established and named as O-Hollow, O-Interface, OLa-Hollow and OLa-Interface, respectively.

(4) The adhesive work of four interface models is as follows: $Wad_{OHollow} > Wad_{O\text{-}Interface} > Wad_{OLa\text{-}Interface} > Wad_{OLa\text{-}Hollow}$. The interface energy of four interface models is as follows: $\gamma_{O\text{-}Hollow} < \gamma_{OInterface} < \gamma_{OLa\text{-}Hollow} < \gamma_{OLa\text{-}Interface}$. Among them, the adhesive work of O-Hollow interface is the largest (0.995 J/m^2) and its interface energy is the smallest (3.055 J/m^2)

(5) The main bonding types of O-Hollow interface is the combination of La-C bonds and Nb-O bonds.

CRediT authorship contribution statement

Wenwei Song: Conceptualization, Methodology, Software, Data curation, Investigation, Writing – original draft. Qizhen He: Formal analysis. Yuguo Zhuo: Funding acquisition, Validation. Wei Shao: Methodology. Silong Zhang: Visualization. Xuejun Ren: Funding acquisition, Conceptualization, Supervision. Qingxiang Yang: Funding acquisition, Project administration, Writing − review & editing, Supervision.

Declaration of Competing Interest

The authors declare that they have no known competing financial interests or personal relationships that could have appeared to influence the work reported in this paper.

Data availability: Data will be made available on request.

Acknowledgements

The authors would like to express their gratitude for projects supported by the National Natural Science Foundation of China (No. 51771167) and EU H2020 Marie Skłodowska-Curie project “i-Weld” (No. 823786).

References

[1] D. Sun, L. Zhu, Y. Cai, et al., Tribology comparison of laser-cladded CrMnFeCoNi coatings reinforced by three types of ceramic (TiC/NbC/B4C)[J], Surf. Coat. Technol. 450 (2022), 129013.
[2] D. Demirskyi, Y. Sakka, O. Vasylkiv, High-temperature reactive spark plasma consolidation of TiB2–NbC ceramic composites[J], Ceram. Int. 41 (9) (2015) 10828–10834.
[3] G.P. Abdel Rahim, J.A. Rodriguez, Structural and electronic properties of ScC and NbC: A first principles study[C]//Solid State Phenomena, Trans. Tech. Publ. Ltd 194 (2013) 276–279.
[4] Q. Li, Y. Lei, H. Fu, Laser cladding in-situ NbC particle reinforced Fe-based composite coatings with rare earth oxide addition[J], Surf. Coat. Technol. 239 (2014) 102–107.
[5] Y. Zhao, L. Chen, J. Sun, et al., Microstructure evolution and wear resistance of insitu synthesized (Ti, Nb) C ceramic reinforced Ni2O4 composite coatings[J], Ceram. Int. 48 (12) (2022) 17518–17528.
[6] H. Zuhailawati, H.M. Salihin, Y. Mahani, Microstructure and properties of copper composite containing in situ NbC reinforcement: Effects of milling speed[J], J. Alloy. Compd. 489 (2) (2010) 369–374.
[7] N. Zhao, L. Wang, R. Xu, et al., Microscopic and macroscopic interfacial studies of NbC reinforcement layer on GCr15 bearing steel surface prepared by in-situ reaction method[J], Vacuum 200 (2022), 110992.
[8] Y. Zhang, R. Song, Y. Pei, et al., The formation of TiC–NbC core-shell structure in hypereutectic high chromium cast iron leads to significant refinement of primary M7C3[J], J. Alloy. Compd. 824 (2020), 153806.
[9] B. Lu, X. Cui, Y. Li, et al., Microstructure, bonding properties and the basis of pinning effect of in-situ NbC reinforced Co50 composite coating by plasma cladding[J], Surf. Coat. Technol. 319 (2017) 155–163.
[10] T. Zeng, S. Zhang, X. Shi, et al., Effect of NbC and VC carbides on microstructure and strength of high-strength low-alloyed steels for oil country tubular goods[J], Mater. Sci. Eng.: A 824 (2021), 141845.
[11] K.L. Wang, Q.B. Zhang, M.L. Sun, et al., Rare earth elements modification of laserclad nickel-based alloy coatings[J], Appl. Surf. Sci. 174 (3–4) (2001) 191–200.
[12] Z. Zhang, X. Lu, B. Han, et al., Rare earth effect on microstructure, mechanical and tribological properties of CoCrW coatings[J], Mater. Sci. Eng.: A 444 (1–2) (2007) 92–98.
[13] M.J. Whitehouse, J.P. Platt, Dating high-grade metamorphism—constraints from rare-earth elements in zircon and garnet[J], Contrib. Mineral. Petrol. 145 (1) (2003) 61–74.
[14] C. Liu, R.I. Revilla, Z. Liu, et al., Effect of inclusions modified by rare earth elements (Ce, La) on localized marine corrosion in Q460NH weathering steel[J], Corros. Sci. 129 (2017) 82–90.

[15] L.M. Wang, Q. Lin, L.J. Yue, et al., Study of application of rare earth elements in advanced low alloy steels[J], J. Alloy. Compd. 451 (1–2) (2008) 534–537.
[16] S.X. Luo, Z.M. Shi, N.Y. Li, et al., Crystallization inhibition and microstructure refinement of Al-5Fe alloys by addition of rare earth elements[J], J. Alloy. Compd. 789 (2019) 90–99.
[17] W. Xiao, Y. Shen, L. Wang, et al., The influences of rare earth content on the microstructure and mechanical properties of Mg–7Zn–5Al alloy[J], Mater. Des. 31 (7) (2010) 3542–3549.
[18] K. Xia, W. Li, C. Liu, Effects of addition of rare earth element Gd on the lamellar grain sizes of a binary Ti-44Al alloy[J], Scr. Mater. 41 (1) (1999) 67–73.
[19] H. Zhuang, Q. Zhang, D. Zhang, Microstructure and Tribological Properties of NiBased Laser-Clad Coatings by Rare Earth Modification[J], J. Therm. Spray. Technol. 30 (5) (2021) 1410–1431.
[20] K. Hantzsche, J. Bohlen, J. Wendt, et al., Effect of rare earth additions on microstructure and texture development of magnesium alloy sheets[J], Scr. Mater. 63 (7) (2010) 725–730.
[21] S. Liang, H. Wang, Y. Li, et al., Rare-earth based nanomaterials and their composites as electrode materials for high performance supercapacitors: a review [J], Sustain. Energy Fuels 4 (8) (2020) 3825–3847.
[22] Z. Zhao, S. Zhe, H. Chen, et al., Renewable Biomass-derived Carbon-based Hosts for Lithium-Sulfur Batteries[J], Sustain. Energy Fuels (2022).
[23] W. Jiang, Z. Fan, Y. Dai, et al., Effects of rare earth elements addition on microstructures, tensile properties and fractography of A357 alloy[J], Mater. Sci. Eng.: A 597 (2014) 237–244.
[24] Y.F. Zhou, Y.L. Yang, X.W. Qi, et al., Influence of La2O3 addition on microstructure and wear resistance of Fe-Cr-C cladding formed by arc surface welding[J], J. Rare Earths 30 (10) (2012) 1069–1074.
[25] X.Y. Jiao, W.T. Fu, W. Shao, et al., First-principles calculation on γ-Fe/La2O3 interface properties and austenite refinement mechanism by La2O3[J], Mater. Chem. Phys. 259 (2021), 124194.
[26] Q. Li, Y. Lei, H. Fu, Laser cladding in-situ NbC particle reinforced Fe-based composite coatings with rare earth oxide addition[J], Surf. Coat. Technol. 239.
[27] M. Quazi, M.A. Fazal, A. Haseeb, et al., Effect of rare earth elements and their oxides on tribo-mechanical performance of laser claddings: A review[J], J. Rare Earths 34 (6) (2016) 549–564.
[28] Z.J. Shi, S. Liu, J. Guo, et al., Investigation on heterogeneous nucleation substrate of Y2O3 as NbC in hypereutectic Fe–Cr–C hardfacing coating by experiment and first-principles calculation[J], J. Mater. Sci. 54 (14) (2019) 10102–10118.
[29] W.W. Song, Q.Z. He, L.X. Rao, et al., Heterogeneous nucleation interface between LaAlO3 and niobium carbide: First-principles calculation[J], Appl. Surf. Sci. 606 (2022), 154731.
[30] H. Xing, P. Hu, S. Li, et al., Adsorption and diffusion of oxygen on metal surfaces studied by first-principle study: A review[J], J. Mater. Sci. Technol. 62 (2021) 180–194.
[31] H. Zhao, Y. Yang, X. Shu, et al., Adsorption of organic molecules on mineral surfaces studied by first-principle calculations: A review[J], Adv. Colloid Interface Sci. 256 (2018) 230–241.
[32] X. Guo, Y. Zhang, Y.G. Jung, et al., Ideal tensile strength and shear strength of ZrO2 (111)/Ni (111) ceramic-metal Interface: A first principle study[J], Mater. Des. 112 (2016) 254–262.
[33] F. Ling, W. Li, L. Ye, The synergistic effect of non-metal doping or defect engineering and interface coupling on the photocatalytic property of g-C3N4: Firstprinciple investigations[J], Appl. Surf. Sci. 473 (2019) 386–392.
[34] H. Xue, X. Wei, W. Guo, et al., Bonding mechanism study of active Ti element and α-Al2O3 by using first-principle calculation[J], J. Alloy. Compd. 820 (2020), 153070.

[35] G. Kresse, J. Hafner, Ab initio molecular dynamics for liquid metals[J], Phys. Rev. B 47 (1) (1993) 558.
[36] G. Kresse, J. Hafner, Ab initio molecular-dynamics simulation of the liquidmetal–amorphous-semiconductor transition in germanium[J], Phys. Rev. B 49 (20) (1994) 14251.
[37] G. Kresse, J. Furthmüller, Efficient iterative schemes for ab initio total-energy calculations using a plane-wave basis set[J], Phys. Rev. B 54 (16) (1996) 11169.
[38] J.P. Perdew, K. Burke, M. Ernzerhof, Generalized gradient approximation made simple[J], Phys. Rev. Lett. 77 (18) (1996) 3865.
[39] P.E. Blochl, ¨ Projector augmented-wave method[J], Phys. Rev. B 50 (24) (1994) 17953.
[40] G. Kresse, D. Joubert, From ultrasoft pseudopotentials to the projector augmentedwave method[J], Phys. Rev. B 59 (3) (1999) 1758.
[41] H.J. Monkhorst, J.D. Pack, Special points for Brillouin-zone integrations[J], Phys. Rev. B 13 (12) (1976) 5188.
[42] N. Sulaiman, Y. Yulizar, D.O.B. Apriandanu, Eco-friendly method for synthesis of La2O3 nanoparticles using Physalis angulata leaf extract[C]//AIP conference proceedings, AIP Publ. LLC 2023 (1) (2018), 020105.
[43] V. Wang, N. Xu, J.C. Liu, et al., VASPKIT: A user-friendly interface facilitating highthroughput computing and analysis using VASP code[J], Comput. Phys. Commun. 267 (2021), 108033.
[44] X. Wang, M. Wang, H. Song, et al., A simple sol–gel technique for preparing lanthanum oxide nanopowders[J], Mater. Lett. 60 (17–18) (2006) 2261–2265.
[45] M. Moothedan, K.B. Sherly, Synthesis, characterization and sorption studies of nano lanthanum oxide[J], J. Water Process Eng. 9 (2016) 29–37.
[46] R. Jha, V.P.S. Awana, Vacuum encapsulated synthesis of 11.5 K NbC superconductor[J], J. Supercond. Nov. Magn. 25 (5) (2012) 1421–1425.
[47] R. Gaillac, P. Pullumbi, F.X. Coudert, ELATE: an open-source online application for analysis and visualization of elastic tensors[J], J. Phys.: Condens. Matter 28 (27) (2016), 275201.
[48] B.L. Bramfitt, The effect of carbide and nitride additions on the heterogeneous nucleation behavior of liquid iron[J], Metall. Trans. 1 (7) (1970) 1987–1995.
[49] J.C. Boettger, Nonconvergence of surface energies obtained from thin-film calculations[J], Phys. Rev. B 49 (23) (1994) 16798.
[50] V. Fiorentini, M. Methfessel, Extracting convergent surface energies from slab calculations[J], J. Phys.: Condens. Matter 8 (36) (1996) 6525.

Table 1
Elastic constants of La_2O_3.

	Bulk modules (K)	Young's modulus (E)	Shear modulus (G)	Poisson's ratio (μ)
La_2O_3	115.63 GPa	102.70 GPa	37.98 GPa	0.35

Table 2
Elastic anisotropy of La_2O_3.

La_2O_3	Bulk modules (GPa)		Linear coefficient (TPa^{-1})		Shear modulus (GPa)		Poisson's ratio	
	Emin	Emax	βmin	βmax	Gmin	Gmax	μmin	μmax
Values	46.16	201.49	1.79	5.44	15.36	81.80	-0.16	0.97
Anisotropy	4.37		3.04		5.33		∞	

Table 3
Two-dimensional lattice mismatch degree of La_2O_3/NbC interface.

Matching face	La_2O_3 ($1\bar{1}0$)//NbC ($1\bar{1}0$)			La_2O_3 (001)//NbC (100)			La_2O_3 (100)//NbC (100)		
[uvw] La_2O_3	[$00\bar{1}$]	[110]	[$11\bar{1}$]	[100]	[120]	[110]	[110]	[$1\bar{1}0$]	[100]
[uvw]NbC	[110]	[001]	[111]	[$01\bar{1}$]	[011]	[010]	[$1\bar{1}0$]	[011]	[010]
θ(°)	0	0	2.88	0	0	15	0	0	9.736
d La_2O_3 (Å)	6.204	3.935	7.346	3.935	6.815	3.935	6.204	6.815	9.216
dNbC(Å)	6.373	4.506	7.805	6.373	6.373	4.506	6.373	6.373	4.506
δ(%)	7.1			18.0			20.3		

Table 4
Surface energy of $La_2O_3(1\bar{1}0)$ surface models with OLa-Terminated and O-Terminated.

Layer	4	7	10	13	16
$\sigma_{OLa\text{-}Terminated}(J/m^2)$	2.03	2.07	2.07	2.07	2.08
$\sigma_{O\text{-}Terminated}(J/m^2)$	1.06	0.63	1.08	1.09	1.09

Table 5
Surface energy of NbC($1\bar{1}0$) surface models with NbC-Terminated.

Layer	5	7	9	11	13
$\sigma_{NbC\text{-}Terminated}(J/m^2)$	3.13	3.17	2.86	2.97	2.88

Table 6
Adhesive work of $La_2O_3(1\bar{1}0)$/NbC($1\bar{1}0$) interface models.

Interface	O-Hollow	O-Interface	OLa-Hollow	OLa-Interface
$W_{ad}(J/m^2)$	0.995	0.949	-0.032	-0.033

Table 7
Interface energy of $La_2O_3(1\bar{1}0)$/NbC($1\bar{1}0$) interface models.

Interface	O-Hollow	O-Interface	OLa-Hollow	OLa-Interface
$\gamma(J/m^2)$	3.055	3.101	5.073	5.074

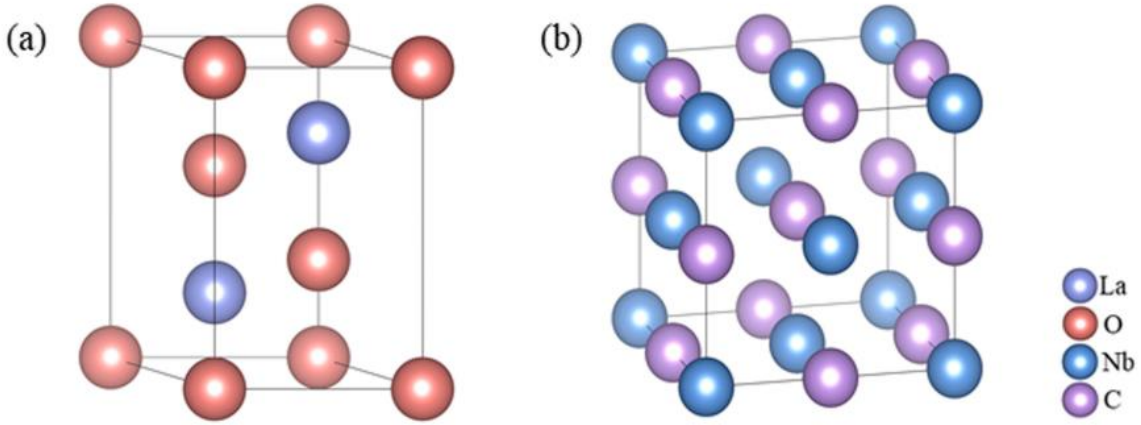

Fig. 1. Crystal structure model of La2O3 and NbC, (a) La2O3; (b) NbC.

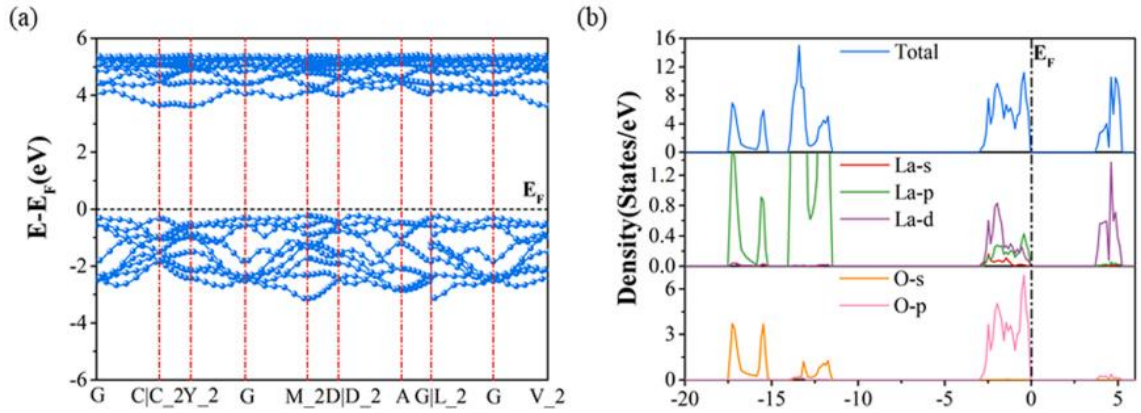

Fig. 2. Band and DOS of La2O3, (a) Band diagram; (b) DOS

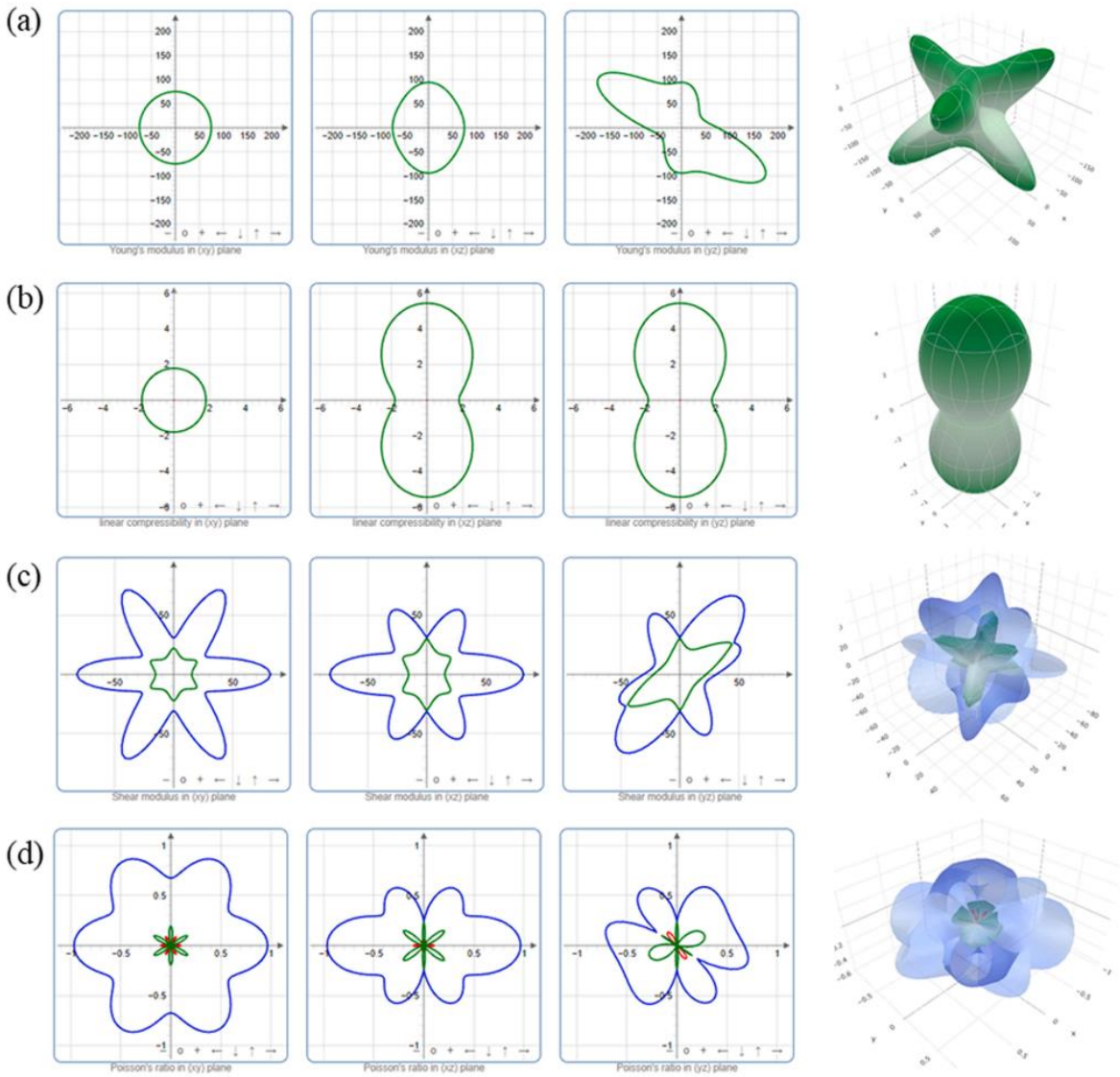

Fig. 3. 2D and 3D distribution of elastic constants of La2O3, (a) Young's modulus; (b) linear coefficient; (c) shear modulus; (d) Poisson's ratio.

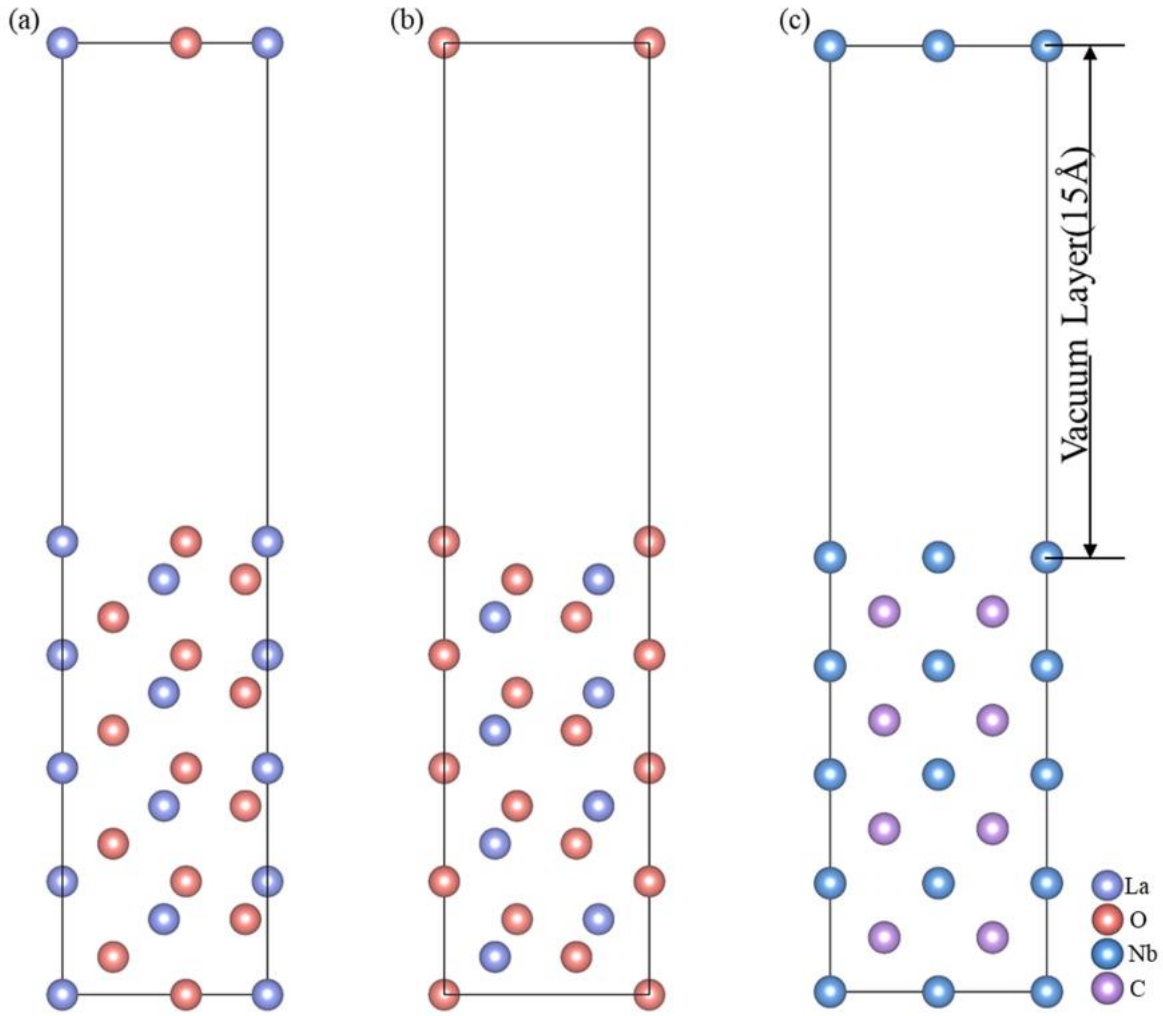

Fig. 4. Schematic diagram of surface models of La2O3 and NbC, (a) OLa-Termiated surface models of La2O3(110) planes; (b) O-Termiated surface models of La2O3(110) planes; (c) NbC-Terminated surface models of NbC(110) planes.

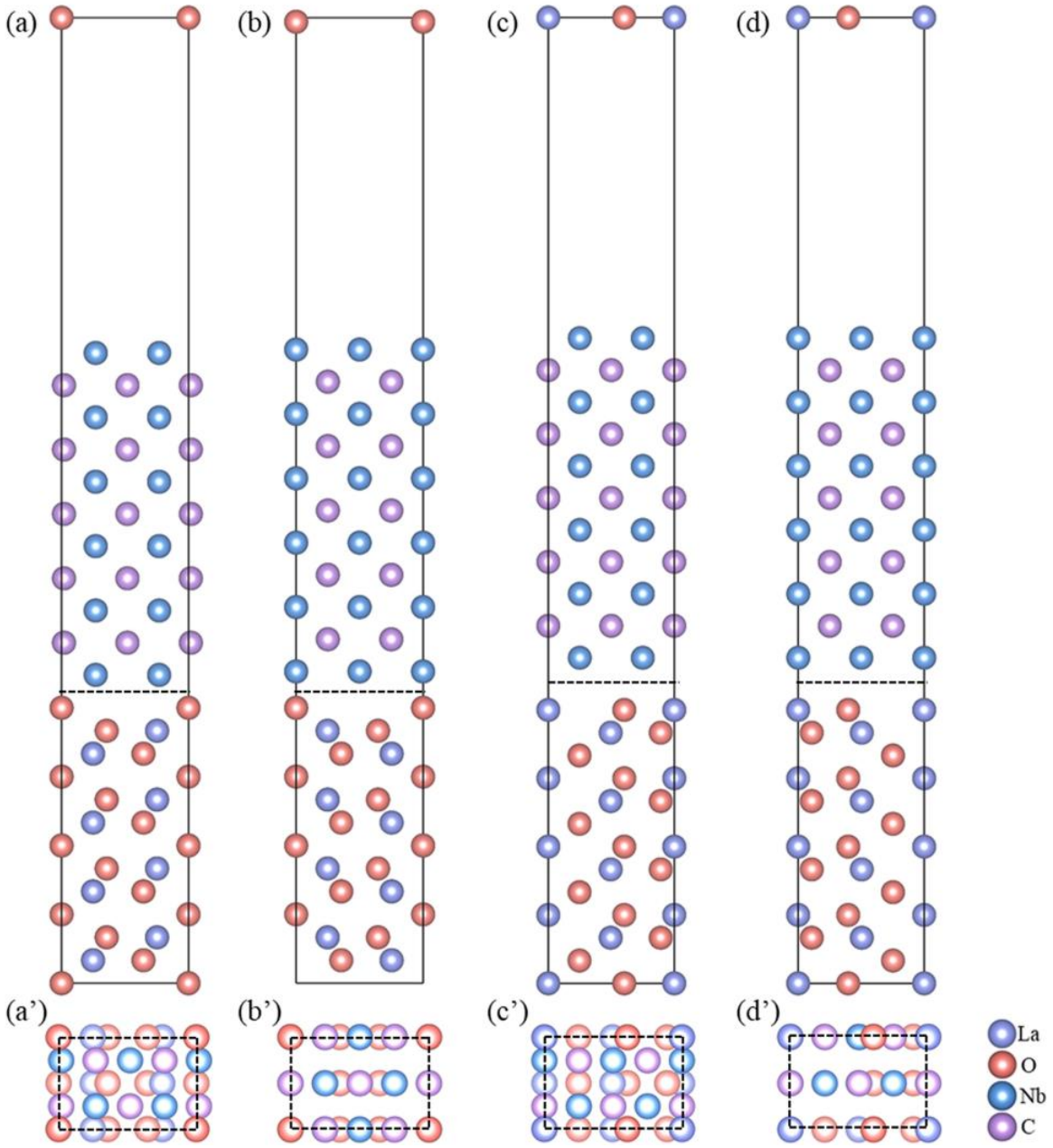

Fig. 5. Four types of interfacial structures and their top views, (a,a′) O-Hollow; (b,b′) O-Interface; (c,c′) OLa-Hollow; (d,d′) OLa-Interface.

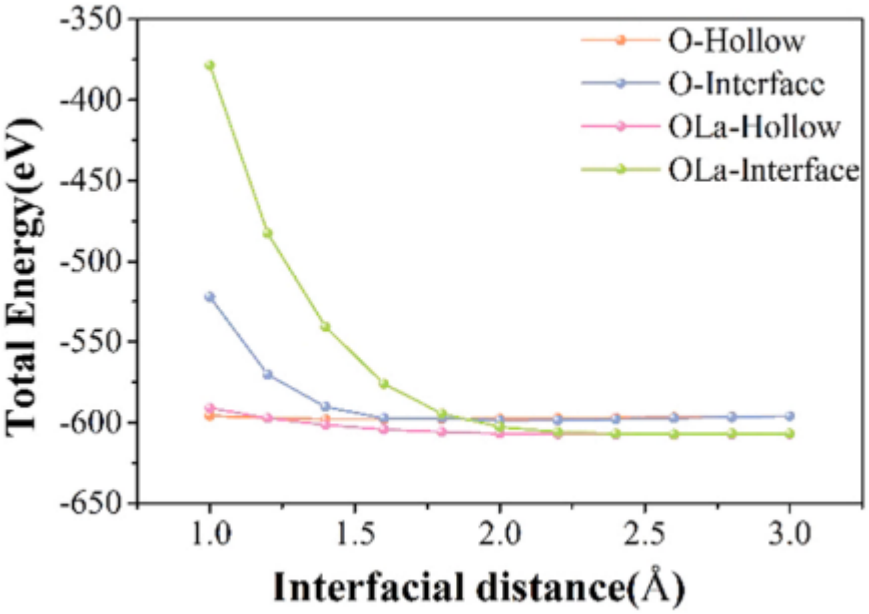

Fig. 6. Variation curves of energy and interface spacing for four interface models.

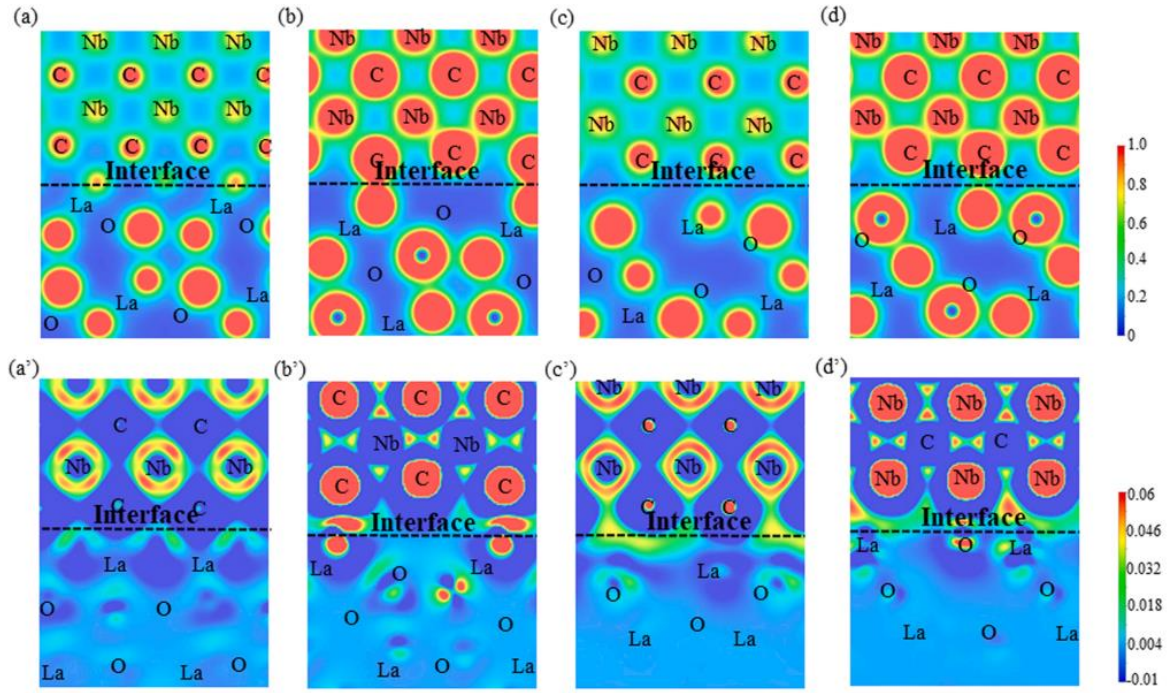

Fig. 7. Electronic structures of the La2O3(110)/NbC(110) interface models, Charge density map: (a) O-Hollow (b) O-Interface (c) OLa-Hollow (d) OLa-Interface, Differential charge density map: (a′) O-Hollow (b′) O-Interface (c′) OLa-Hollow (d′) OLa-Interface.

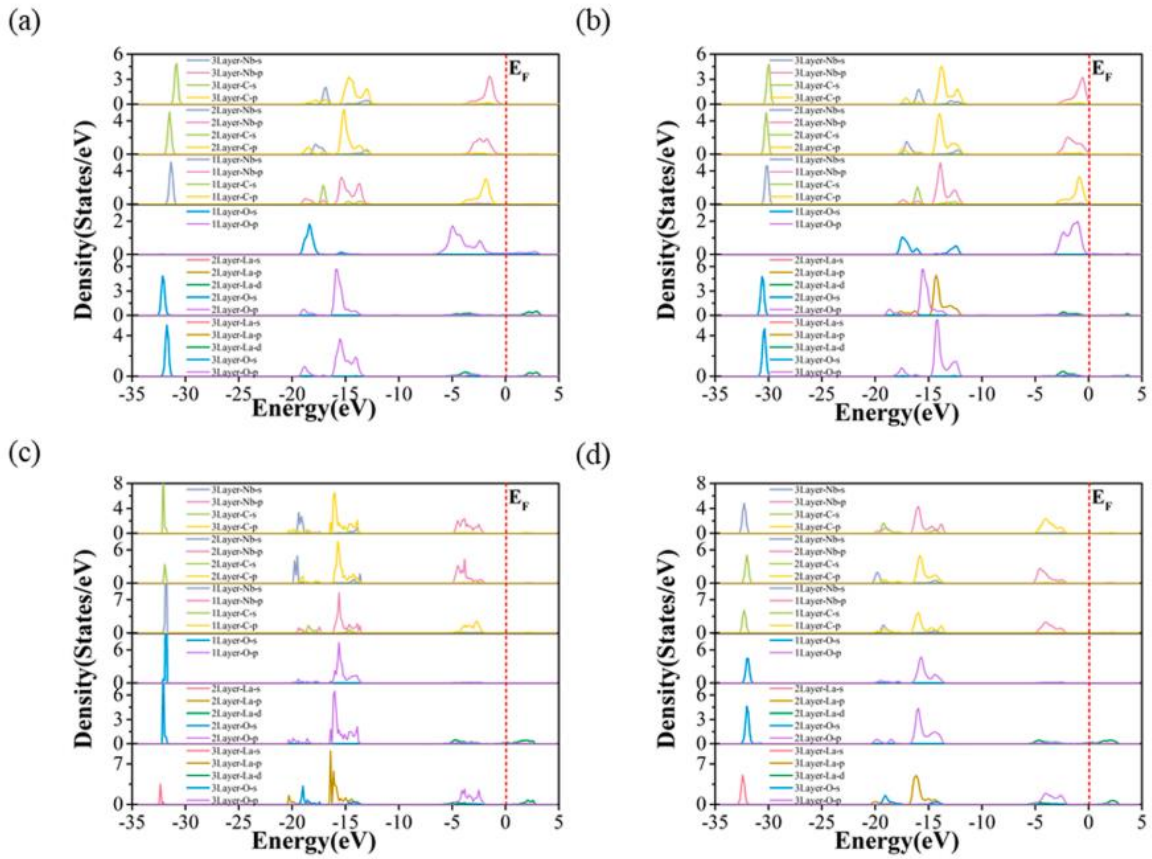

Fig. 8. PDOS of four interface structure, (a,a′) O-Hollow; (b,b′) O-Interface; (c,c′) OLa-Hollow; (d,d′) OLa-Interface.